Journal of Alloys and Compounds 1020 (2025) 179361

Contents lists available at ScienceDirect

Journal of Alloys and Compounds

journal homepage: www.elsevier.com/locate/jalcom

Operative slip system and dislocation behavior in a brittle refractory high-entropy alloy with the B2 ordered structure

Shu Han [a,1], Stephan Laube [b,1], Zhenghao Chen [a,*], Alexander Kauffmann [b,*], Martin Heilmaier [b,*], Haruyuki Inui [a,*]

[a] Department of Materials Science and Engineering, Kyoto University, Sakyo-ku, Kyoto 606-8501, Japan
[b] Institute for Applied Materials (IAM), Karlsruhe Institute of Technology (KIT), Kaisestraße 12, Karlsruhe 76131, Germany

ARTICLE INFO

Keywords:
Refractory high-entropy alloys
B2-ordered structure
Micropillar
Plastic deformation
Slip
Dislocation structure

ABSTRACT

The plastic deformation behavior of a B2-ordered TiCrMo-15Al refractory high-entropy alloy (RHEA) has been investigated as a function of crystal orientation and specimen size by micropillar compression at room temperature, in an attempt to understand the origin for the brittle behavior of the B2 compound based on the identified operative slip systems and dislocation structures. Plastic flow is observed even at room temperature for all orientations investigated with the slip direction always being along <1 1 1>. While the slip plane is {1 1 0} in a wide orientation range, it is {1 1 2} in the narrow orientation range close to the twinning and anti-twinning shear directions. The dislocation structure is characterized by the preference of <1 1 1> screw dislocations, strongly indicating that the deformation is controlled by the Peierls mechanism. The < 1 1 1> dislocation is found to widely dissociate into two-coupled collinear 1/2<1 1 1> partial dislocations. The anti-phase boundary (APB) energy is estimated to be 44 mJ/m^2, which is quite low and is considered to be the origin for the preference not only of the <1 1 1> slip direction but also of the {1 1 0} slip plane. The room-temperature brittleness is thus concluded not to be caused by the lack of the sufficient number of independent slip systems (von Mises criterion).

1. Introduction

High-entropy alloys (HEAs) with the body-centered cubic (BCC) structure, also commonly referred to as the refractory high-entropy alloys (RHEAs) due to their high-melting temperature constituents, have garnered significant attention over the past decades owing to their high yield strength at elevated temperatures. This makes them a highly promising candidates for the next-generation high-temperature structural materials that could potentially replace the existing Ni-based superalloys [1–4]. In the quest toward their practical applications, some attempts were made in recent years to lower the overall density and thereby to enhance the specific strength of RHEAs by incorporating lightweight elements such as Al [5–10]. These Al-added RHEAs are found, however, to incorporate some other phases such as the B2 (ordered BCC) phase in many cases due to the reduced BCC phase stability. Unfortunately, these B2 phase-containing RHEAs usually suffer from the room-temperature brittleness, even when the BCC+B2 two-phase microstructure is tuned to mimic the γ+γ' cuboidal microstructure of Ni-based superalloys, such as those found in the Ti-V-Zr-Nb-Ta-Al system [5,6,8,11]. The room-temperature brittleness of these BCC+B2 two-phase RHEAs may arise in part from the brittleness of the constituent B2 intermetallic phase itself. However, almost nothing is known about how and why the B2 intermetallic phase in these RHEAs is brittle at room temperature. This is due to the lack of fundamental studies to elucidate the deformation mechanisms (such as the operative slip systems and their critical resolved shear stresses (CRSSs)) of the B2 intermetallic phase.

Since the B2 ordered structure is based on the BCC lattice, the closest-packed direction is <1 1 1>, as in the BCC structure. Because of the B2 ordering, the shortest translation vector along this direction is <1 1 1>, twice that (1/2<1 1 1>) for the BCC structure. Slip along <1 1 1> is thus carried by the motion of the dislocation with the Burgers vector $\boldsymbol{b}$ = <1 1 1> on either the {1 1 0} or {1 1 2} slip plane, and the <1 1 1> dislocation is known to dissociate into two identical superpartial dislocations

* Corresponding authors.
E-mail addresses: chen.zhenghao.6e@kyoto-u.ac.jp (Z. Chen), alexander.kauffmann@kit.edu (A. Kauffmann), martin.heilmaier@kit.edu (M. Heilmaier), inui.haruyuki.3z@kyoto-u.ac.jp (H. Inui).
[1] These two authors contributed equally to this work.

https://doi.org/10.1016/j.jallcom.2025.179361
Received 27 November 2024; Received in revised form 9 February 2025; Accepted 21 February 2025
Available online 23 February 2025

with $\boldsymbol{b}$ = 1/2<1 1 1> separated by an antiphase boundary (APB) [12,13]. The APB energy is known to increase with the increase in the ordering energy among the constituent elements. When the APB energy is too high for the above dislocation dissociation to occur, the slip direction is considered to change to <0 0 1>, the second closest-packed direction as well as the shortest translation vector in the B2 structure [12,13]. As there are no stable local mimima in stacking fault energy in any slip planes available for the dislocation with $\boldsymbol{b}$ = <0 0 1>, the <0 0 1> dislocation is considered to move as a perfect dislocation without any dissociation preferentially on the {1 1 0} slip plane. Of importance to note is that the <0 0 1> slip vector offers only three independent slip systems, which is not sufficient to satisfy the von Mises criterion for general plasticity of polycrystals, unlike the <1 1 1> slip vector does. Therefore, the B2 intermetallic compounds (such as NiAl [14] and CoTi [15]) that exhibit slip along <0 0 1> are generally brittle in polycrystals at room temperature, while those (CuZn [16], FeAl [17], and FeCo [18]) that exhibit slip along <1 1 1> are generally ductile. This indicates that the identification of slip direction is the first step to (i) identify the deformation mechanism of the B2 compounds and (ii) thereby to understand why and how the B2 intermetallic phase in these RHEAs is brittle at room temperature.

In our previous studies [19,20], we have found that a single-phase RHEA with the B2 ordered structure, 85(TiCrMo)-15Al (at%, abbreviated with TiCrMo-15Al) exhibits a yield strength of as high as 1200 MPa even at 1073 K but a brittle behavior at room temperature, indicating that this B2 single-phase RHEA is a suitable example to investigate the brittle issues of the B2 intermetallic phase in many different RHEAs so far reported. As no other deformation mechanisms than dislocation slip was identified in this compound, we investigate the plastic deformation behavior of single crystals of TiCrMo-15Al with the B2 structure as a function of crystal orientation and specimen size by micropillar compression tests at room temperature, to elucidate the slip and dislocation characteristics and thereby one potential contribution for the room-temperature brittleness through identifying the operative slip systems and their CRSSs. We also evaluate the APB energy from transmission electron microscopy (TEM) observations, to discuss the reason for the slip direction choice and thereby the reason for the room-temperature brittleness.

2. Experimental procedures

Polycrystalline ingots were synthesized through repetitive arc-melting the constituent elements, followed by a heat treatment to ensure homogeneity and microstructure of the B2 single phase (Fig. 1), as detailed in Ref. [19]. The concentrations of Mo, Ti, Cr and Al were determined by inductively coupled plasma-optical emission spectrometry and carrier gas hot extraction to be 29.5, 27.8, 27.7 and 15.0 at%, respectively. The concentrations of O and N impurities were 231 ± 50 and ≤ 0.5 wt.-ppm, respectively. Chemical homogeneity was established by a homogenization treatment at 1200 °C for 20 h with slow furnace cooling at 100 K/h. The initial dislocation density in the micropillar specimens is expectedly low. Microstructure observations and orientation determination were made with a JEOL JSM-7001FA scanning electron microscope (SEM) equipped with an electron backscatter diffraction (EBSD) system. Single-crystal micropillar specimens with a square cross-section having an edge length of 1–10 μm and an aspect ratio of 2–3 were prepared with a JEOL JIB-4000 focused ion beam (FIB) apparatus at an operating voltage of 30 kV. Five different compression-axis orientations shown in Fig. 1 were selected. The Schmid factors for the $(\bar{1}\ 0\ 1)[1\ 1\ 1]$ slip (m_1) and $(\bar{1}\ 1\ 0)[0\ 0\ 1]$ slip (m_2) and their ratio for each orientation are tabulated in Table 1 together with the angle χ between the maximum resolved shear stress plane (MRSSP) and $(\bar{1}\ 0\ 1)$ in the ψ-χ relation, which is usually used to describe the anisotropic deformation behavior of [1 1 1] slip in BCC metals and alloys (ψ is the angle between the actually observed slip plane and $(\bar{1}\ 0\ 1)$) [4,21–23]. For all specimens, [1 1 1], one of the two possible slip directions, was set on one of the two orthogonal side surfaces to facilitate the slip direction determination. Compression tests were conducted for micropillar specimens with a flat punch indenter tip on an Agilent Technologies Nano Indenter G200 nanomechanical tester at room temperature in the displacement-rate-controlled mode at a nominal strain rate of 1×10^{-4} s^{-1}. Deformation microstructures were examined by SEM and transmission electron microscopy (TEM) with a JEOL JEM-2000FX electron microscope operated at 200 kV. These foils

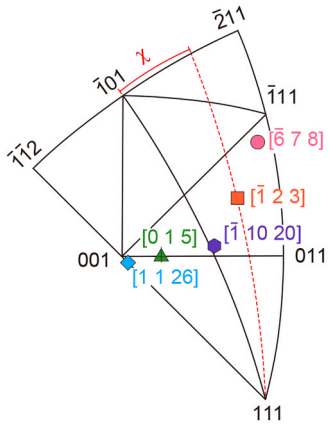

Fig. 2. Compression-axis orientations investigated.

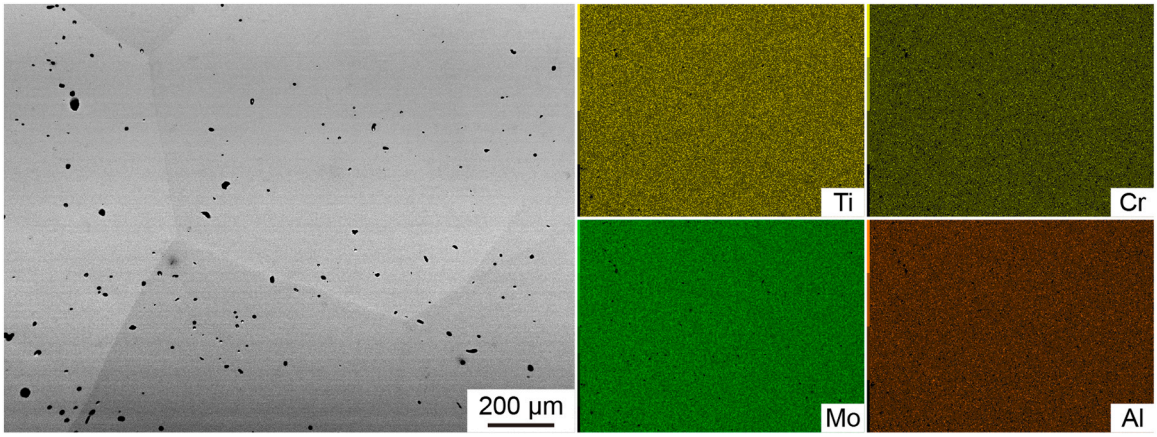

Fig. 1. Backscattered electron (BSE) image (left side) and corresponding energy dispersive x-ray spectroscopy (EDS) maps (right side) of the same field of view. Black features are pores related to the Kirkendall effect during homogenization treatment.

Table 1
χ angle, Schmid factors for $(\bar{1}\ 0\ 1)[1\ 1\ 1]$ slip (m_1) and $(\bar{1}\ 1\ 0)[0\ 0\ 1]$ slip (m_2) as well as their ratio for each compression-axis orientation.

compression-axis orientation	χ angle	Schmid factor for $(\bar{1}\ 0\ 1)[1\ 1\ 1]$ slip (m_1)	Schmid factor for $(\bar{1}\ 1\ 0)$ $[0\ 0\ 1]$ slip (m_2)	m_2/m_1
$[\bar{6}\ 7\ 8]$	26°	0.357	0.493	1.38
$[\bar{1}\ 2\ 3]$	16°	0.467	0.454	0.97
$[\bar{1}\ 10\ 20]$	2°	0.496	0.311	0.63
[0 1 5]	−19°	0.471	0.136	0.29
[1 1 26]	−30°	0.455	0.054*	0.12

*: Schmid factor is calculated for (1 1 0)[0 0 1] slip instead of $(\bar{1}\ 1\ 0)[0\ 0\ 1]$ slip because the former exhibits the larger value.

for TEM observations were prepared by a standard FIB lift-out technique [24] with a dual-beam FEI Quanta 3D 200i system equipped with an OmniProbe manipulator.

3. Results

3.1. Stress-strain curves

Typical stress-strain curves obtained for micropillar specimens with [1 1 26], $[\bar{1}\ 10\ 20]$ and $[\bar{6}\ 7\ 8]$ orientations are shown in Fig. 3 for some selected specimen sizes (edge length L). Compression tests were interrupted at a plastic strain level of 1–2 % for the ease of observations of deformation markings. Unlike in the bulk crystal, the present B2 intermetallic compound exhibits plastic flow even at room temperature. The yield stress, defined as the stress at which the first strain burst occurs as indicated by arrows in Fig. 3, tends to decrease with increasing specimen size for all orientations, although the significance of the decrease in yield stress depends on crystal orientation.

3.2. Slip lines

Deformation markings on the specimen surfaces were examined by SEM observations made from a direction inclined from the compression-axis direction by 30°, as shown in Fig. 4. For the $[\bar{6}\ 7\ 8]$-oriented specimen (Fig. 4(a)–(c)), while the deformation markings are clearly observed perpendicularly to the compression axis on the $(\overline{203}\ \overline{86}\ 77)$ surface (Fig. 4(c)), those on the $(\bar{1}\ 14\ \overline{13})$ surface are very faint (Fig. 4(a)). This clearly indicates that [1 1 1] is the slip direction, as this direction is set on the $(\bar{1}\ 14\ \overline{13})$ surface. The fact that this orientation is the most favored for $(\bar{1}\ 1\ 0)[0\ 0\ 1]$ slip over $(\bar{1}\ 0\ 1)[1\ 1\ 1]$ slip when

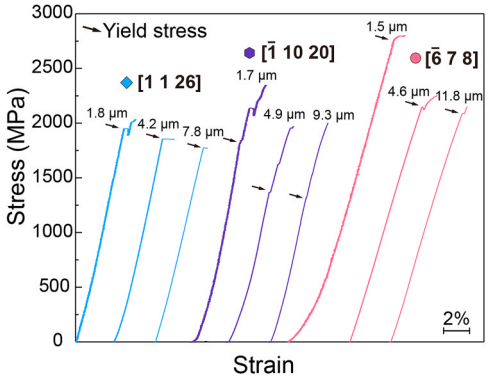

Fig. 3. Typical stress-strain curves for the [1 1 26]-, $[\bar{1}\ 10\ 20]$-, and $[\bar{6}\ 7\ 8]$-oriented micropillar specimens, respectively. The specimen size (mean edge length L) is indicated for each of the curves.

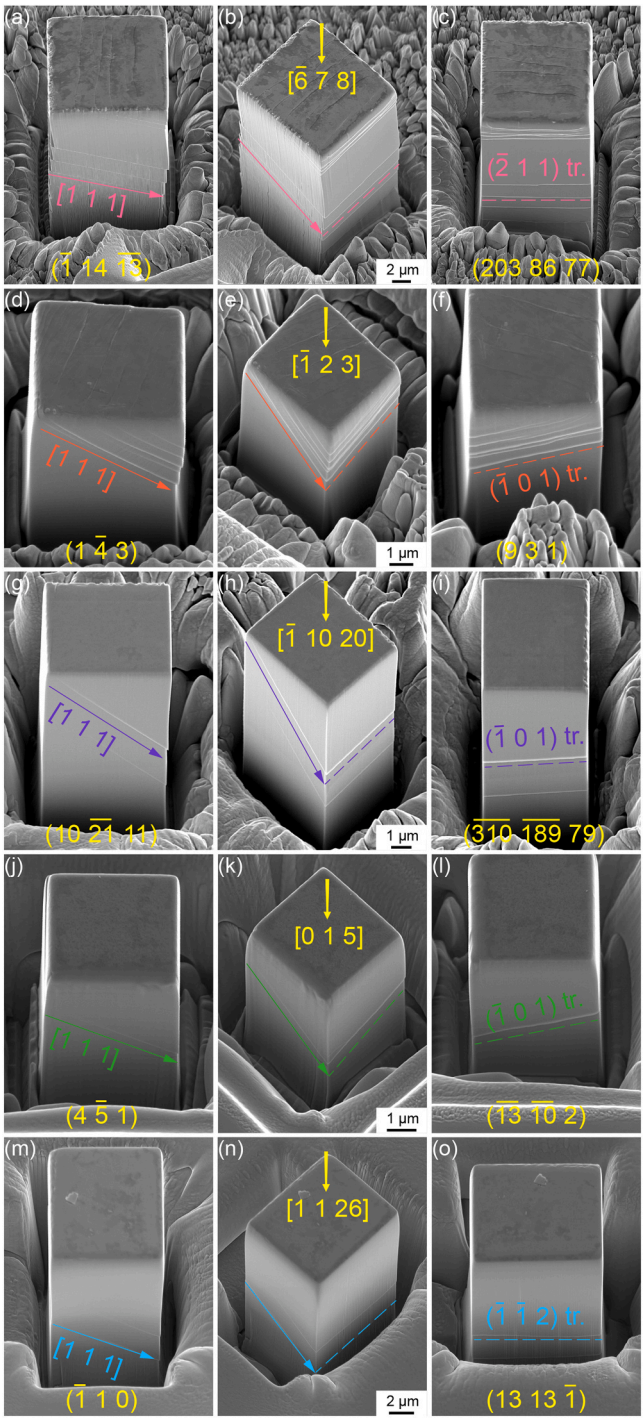

Fig. 4. Slip traces observed on two orthogonal surfaces of micropillar specimens with the compression-axis orientations of (a–c) $[\bar{6}\ 7\ 8]$, (d–f) $[\bar{1}\ 2\ 3]$, (g–i) $[\bar{1}\ 10\ 20]$, (j–l) [0 1 5], and (m–o) [1 1 26].

judged from the m_2/m_1 in Table 1 strongly indicates that [0 0 1] cannot be the slip direction of the present B2 compound for all crystal orientations. This is indeed consistent with the results obtained for other orientations in Fig. 4. Trace analysis on the two orthogonal side faces indicates that the slip plane is $(\bar{2}\ 1\ 1)$, close to the MRSSP plane for this orientation. The slip system thus identified for this orientation is $(\bar{2}\ 1\ 1)$ [1 1 1].

The slip direction is determined to be exclusively [1 1 1] for all other orientations in Fig. 4 similarly from the observations of faint deformation markings on the side surface on which [1 1 1] is set to lie (Fig. 4(d),

(g), (j) and (m)). The slip planes determined from trace analysis for [$\bar{1}$ 10 20]- and [1 1 26]-oriented specimens are respectively ($\bar{1}$ 0 1) (Fig. 4(g)–(i)) and ($\bar{1}$ $\bar{1}$ 2) (Fig. 4(m)–(o)), both of which are very close to their MRSSPs. The slip systems determined to operate for these two orientations are thus ($\bar{1}$ 0 1)[1 1 1] and ($\bar{1}$ $\bar{1}$ 2)[1 1 1], respectively. However, the slip plane determined for [$\bar{1}$ 2 3]- and [0 1 5]-oriented specimens is ($\bar{1}$ 0 1), deviating considerably from their MRSSPs. The slip system determined for these two orientations is thus ($\bar{1}$ 0 1)[1 1 1].

3.3. Dislocation structures

Dislocation structures observed in the deformed [$\bar{1}$ 10 20]- and [$\bar{6}$ 7 8]-oriented micropillar specimens are shown in Fig. 5(a, c) and Figs. (b, d), respectively. These TEM images were taken with thin folis cut parallel to the ($\bar{1}$ 0 1) and ($\bar{2}$ 1 1) slip planes, respectively. All

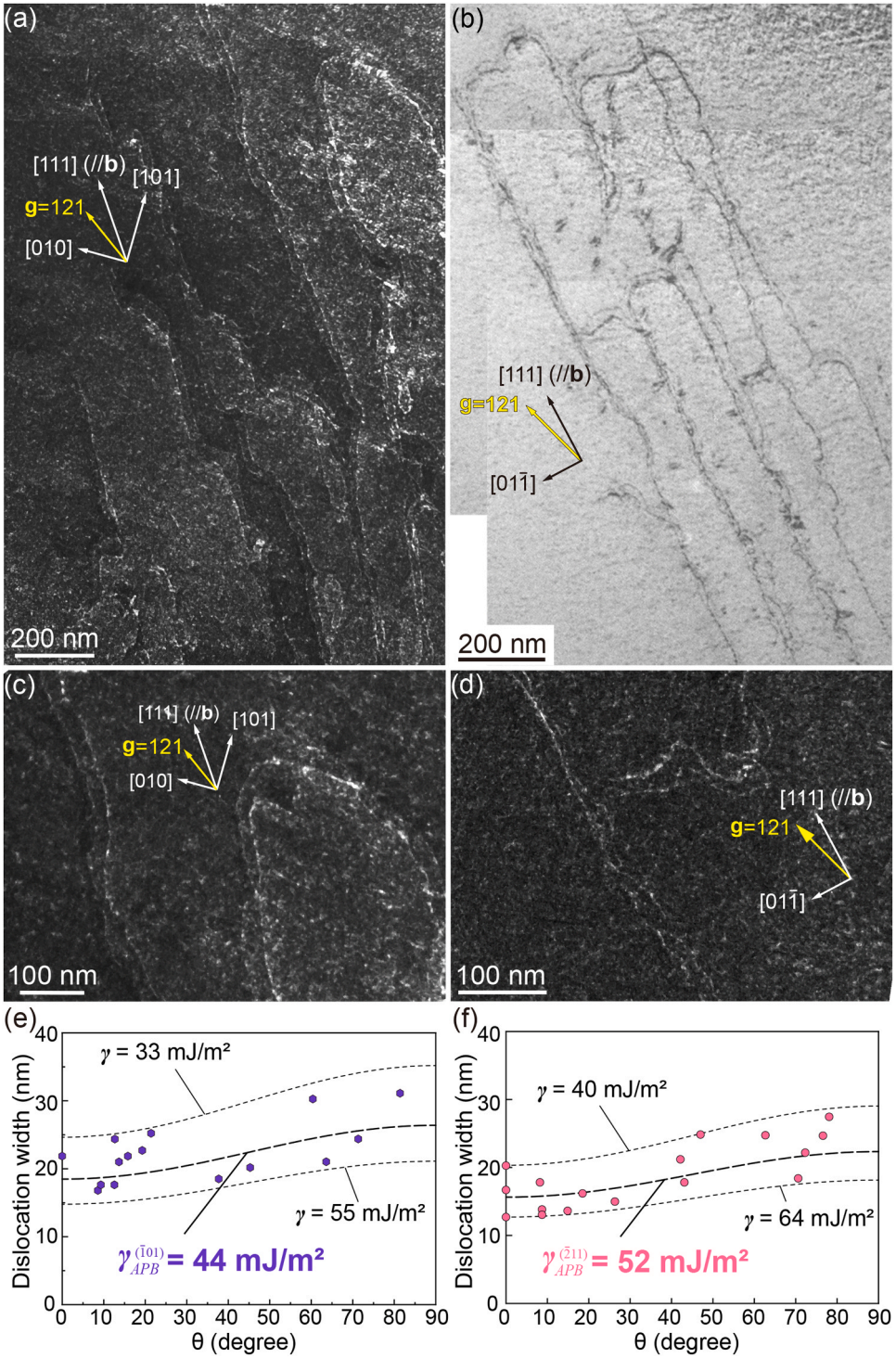

Fig. 5. (a), (b) Dislocation structures in deformed [$\bar{6}$ 7 8]- and [$\bar{1}$ 10 20]-oriented micropillar specimens, respectively. These foils were cut parallel to the ($\bar{1}$ 0 1) and ($\bar{2}$ 1 1) slip planes, respectively. Their magnified WB-DF TEM images are shown respectively in (c), (d). (e), (f) Dissociation widths measured as a function of the angle θ between the dislocation Burgers vector and line vector, from which the APB energy on the ($\bar{1}$ 0 1) and ($\bar{2}$ 1 1) slip planes are deduced.

imaged dislocations in both specimens were confirmed to have a Burgers vector $\boldsymbol{b} = [1\ 1\ 1]$, being consistent with the results of slip trace analysis (Fig. 4). The dislocation densities obtained in the present investigation are estimated to 10^{13}–10^{14} m^{-2} (assuming the foil thickness of ~100 nm as set during FIB machining) regardless of the micropillar orientation tested. This indicates the ability of the material to sufficiently generate dislocations, by nucleation in the first place and by multiplication in the second, even when starting from a dislocation-lean initial condition. A characteristic commonly observed for both specimens is that screw dislocations dominate in the dislocation structure, connected by short edge segments. This clearly indicates that the dislocation motion is controlled by the Peierls mechanism via the kink-pair mechanism, as in many BCC metals and alloys [21,25,26] and B2 intermetallic compounds such as CuZn [27,28] and FeAl [29,30]. Weak-beam dark-field (WBDF) imaging reveals that the dislocation with $\boldsymbol{b} = [1\ 1\ 1]$ dissociate rather widely into two colinear superpartial dislocations with $\boldsymbol{b} = 1/2[1\ 1\ 1]$ separated by an antiphase boundary (APB) (Fig. 4(c) and (d)), as described below.

$$[1\ 1\ 1] \rightarrow 1/2[1\ 1\ 1] + \mathrm{APB} + 1/2[1\ 1\ 1] \quad (1)$$

This dissociation scheme is similar observed in B2-$AlMo_{0.5}NbTa_{0.5}$-TiZr [31]. From the separation distance of the two-coupled superpartial dislocations, we can deduce the APB energy (γ_{APB}) on the $(\bar{1}\ 0\ 1)$ and $(\bar{2}\ 1\ 1)$ planes with the equation described below [32],

$$\gamma_{APB} = \frac{\mu b^2}{2\pi r}\left(\cos^2\theta + \frac{\sin^2\theta}{1-\nu}\right) \quad (2)$$

where μ is the shear modulus, ν is the Poisson's ratio, θ is the angle between the Burgers vector and line vector of the dislocation and r is the separation distance between the two-coupled superpartial dislocations. As shown in Fig. 5(e) and (f), the APB energies (γ_{APB}) on the $(\bar{1}\ 0\ 1)$ and $(\bar{2}\ 1\ 1)$ planes are determined to be 44 and 52 mJ/m^2, respectively, utilizing the values of $\mu = 71$ GPa and $\nu = 0.3$ obtained from our previous work [20]. Simple theoretical estimation based on pairwise interaction energies [13,33] has indicated that in the B2 structure, the APB energy associated with the displacement vector of 1/2<1 1 1> is the lowest on the {1 1 0} plane and that the APB energy on the {1 1 0} plane is lower than that on the {1 1 2} by about 15 % ($\gamma_{APB}^{\{112\}}/\gamma_{APB}^{\{110\}} = 2/\sqrt{3}$). The estimated APB energies on the $(\bar{1}\ 0\ 1)$ and $(\bar{2}\ 1\ 1)$ planes in Fig. 5(e) and (f) are consistent with this. The APB energies estimated for TiCrMo-15Al are quite low, comparable to those reported for CuZn [34–36] and FeAl [37,38] but are considerably lower than those reported for NiAl [35,39] and CoAl [39]. The low APB energy of TiCrMo-15Al is fully consistent with the occurrence of slip along <1 1 1> rather than slip along <0 0 1>.

4. Discussion

4.1. Room-temperature brittleness

The above observations clearly prove that the operative slip system at room temperature in TiCrMo-15Al is $(\bar{1}\ 0\ 1)[1\ 1\ 1]$ for the small $|\chi|$ angles (<25°) and is $(\bar{2}\ 1\ 1)[1\ 1\ 1]$ for the large $|\chi|$ angles (>25°). By contrast, $(\bar{1}\ 1\ 0)[0\ 0\ 1]$ (or $(1\ 1\ 0)[0\ 0\ 1]$) slip is never operative. This strongly suggests that the room-temperature brittleness (limited ductility) of the present B2 intermetallic compound is not caused by the lack of the sufficient number of independent slip systems (von Mises criterion). In fact, B2-Ti_2AlNb that deforms by slip on {110}/{112}<111> is known to be ductile at room temperature [40]. We suspect that the room-temperature brittleness is caused by the high brittle-ductile transition temperature (BDTT) in view of the preferential alignment of <1 1 1> dislocations along the Peierls valley parallel to their screw orientations, leading to a low dislocation mobility (Fig. 5). Unfortunately, deformation twinning that causes twinning-induced plasticity (TWIP) does not occur in the present B2 TiCrMo-15Al, unlike in B2-AlNbTaTiVZr [41]. Grain boundary weakness that occurs either intrinsically or extrinsically (through environmental enbrittlement) cannot be ruled out at present as the cause of the room-temperature brittleness. More work is definitely needed to clarify the cause of the room-temperature brittleness of the present B2 RHEA.

4.2. Operative slip systems and their CRSSs

The observed orientation-dependent slip planes are plotted in Fig. 6 (a) as a function of the angle χ in the form of the ψ-χ plot. While the observed slip plane is close to the MRSSP when χ is very close to 0 and $\pm$ 30°, it is exactly the $(\bar{1}\ 0\ 1)$ plane considerably deviated from their MRSSPs for other χ values ($\chi = +16$ and -19°). The exactly same behavior is observed for CuZn [42], FeAl [43] and FeCo [44] at room temperature. TiCrMo-15Al is thus concluded to prefer {1 1 0} slip over {1 1 2} slip as these other B2 compounds do.

In B2 intermetallic compounds with the slip direction <1 1 1>, it is natural that slip occurs on {1 1 0} as the APB energy with the displacement vector of 1/2<1 1 1> is the lowest on {1 1 0}. However, there is a general tendency that slip on {1 1 2}<1 1 1> is increasingly preferred to slip on {1 1 0}<1 1 1> at room temperature as the ordering energy is increased [45–47]. The ordering energy (E_{order}) is known to be estimated from the critical temperature for ordering (T_c) with $E_{order} = 0.25kT_c$ (k: Bolzmann constant) [48,49]. For example, CuZn (T_c = 734 K) and FeCo (T_c = 1043 K) exhibit slip on {1 1 0}<1 1 1>, while AgMg (T_c = 1093 K) exhibits slip on {1 1 2}<1 1 1>. The T_c of 1237 K determined by calorimetry for TiCrMo-15Al [20], may suggest the preference for {1 1 2}<1 1 1> slip, if the ordering temperature is simply compared with those for the binary B2 compounds listed above. However, the APB energy is also known to be proportional to the ordering energy, if formulated with pairwise interaction energies [13]. The APB energy on {1 1 0} is determined in TiCrMo-15Al to be as low as 44 mJ/m^2, which is much lower than that (98 mJ/m^2 [50]) for AgMg and even that (50–83 mJ/m^2 [34–36]) for CuZn This may indicate that the low APB energy (and thereby the low ordering energy) causes the preference of {1 1 0}<1 1 1> slip in TiCrMo-15Al and at the same time, the empirical formulation of the ordering energy for binary B2 compounds with $E_{order} = 0.25kT_c$ may not be applicable to the present B2 RHEA. We suspect the chemical complexity (not simple binary but four constituent elements of high concentrations) as well as the expected off-stoichiometry are responsible for this.

Values of critical resolved shear stress (CRSS) for $(\bar{1}\ 0\ 1)[1\ 1\ 1]$ slip are calculated in Fig. 6(b) as a function of specimen size (L) with the obtained yield stress and the corresponding Schmid factors for the three orientations, $[\bar{1}\ 10\ 20]$ ($\chi = 2$°), $[\bar{6}\ 7\ 8]$ ($\chi = 26$°) and [1 1 26] (χ = -30°), in Table 1. The CRSS for $(\bar{1}\ 0\ 1)[1\ 1\ 1]$ slip tends to decrease as the specimen size increases following the inverse power-law relationship ($CRSS \propto L^{-n}$) with the power-law exponent, n varying depending on crystal orientation. The power-law exponents n for all three orientations (0.02, 0.26, and 0.17 for [1 1 26], $[\bar{1}\ 10\ 20]$ and $[\bar{6}\ 7\ 8]$ orientations, respectively) are consistent with those (n = 0–0.2) reported in hard and brittle materials [51–53]. The CRSS value obtained for micropillar specimens of FCC and BCC metals is known to usually approach the corresponding bulk value as the specimen size increases to the range of 20–30 μm [54,55], although the relation between the inverse power-law scaling for the specimen-size dependent CRSS and bulk CRSS value has often been discussed along different argumentation chains [56–58]. On that basis, the bulk CRSS values for $(\bar{1}\ 0\ 1)[1\ 1\ 1]$ slip at room temperature are estimated to be 772, 426, and 606 MPa, respectively, as shown in Fig. 6(c). The Schmid law is not valid for $(\bar{1}\ 0\ 1)[1\ 1\ 1]$ slip. This is consistent with anisotropy in yield stress (twinning-anti-twinning asymmetry) often reported for conventional BCC metals and alloys [21,22], in which the CRSS for $(\bar{1}\ 0\ 1)[1\ 1\ 1]$ slip is higher for $\chi = -30$° (the

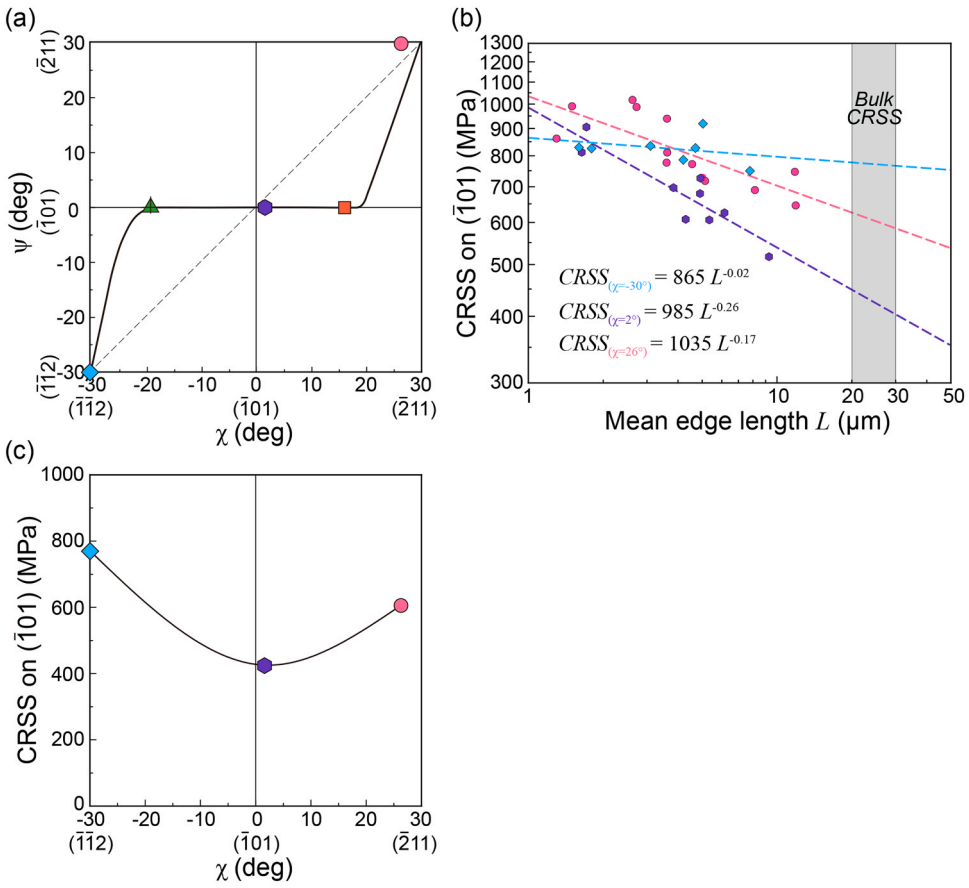

Fig. 6. (a) Orientation-dependent observed slip planes shown in the form of the ψ-χ plot. (b) CRSS values for $(\bar{1}\ 0\ 1)[1\ 1\ 1]$ slip plotted as a function of specimen size (L) calculated with the obtained yield stress and the corresponding Schmid factors for the three orientations, $[\bar{1}\ 10\ 20]$ ($\chi = 2°$), $[\bar{6}\ 7\ 8]$ ($\chi = 26°$) and [1 1 26] ($\chi = -30°$). (c) Compression-axis orientation dependence of the deduced bulk CRSS.

anti-twinning shear direction) than for $\chi = 30°$ (the twinning shear direction).

4.3. Comparison with other B2 compounds

The expected bulk yield stress values at room temperature deduced from the estimated bulk CRSS values multiplied by the Taylor factor M = 3.067 (for {1 1 0} slip) and 2.954 (for {1 1 2} slip) [59] are plotted in Fig. 7(a) as a function of temperature, together with those obtained for bulk polycrystals of TiCrMo-15Al in our previous study [20]. Bulk polycrystals of TiCrMo-15Al can be plastically deformed above 673 K, exhibiting almost a plateau in yield stress (at a level of 1200–1300 MPa) in the temperature range of 673–1073 K. The yield stress at room temperature averaged over the three orientations is 1792 MPa. The strain

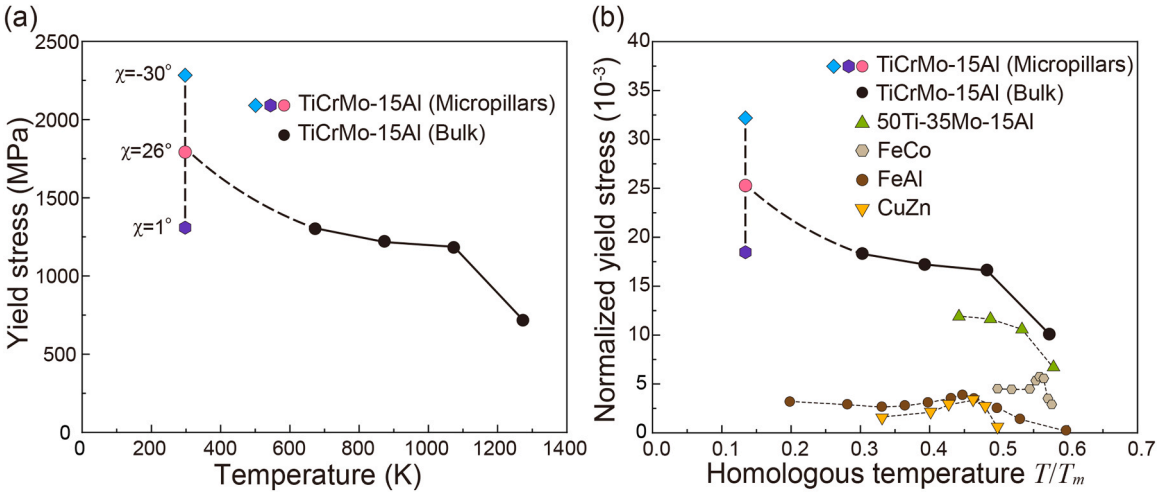

Fig. 7. (a) The expected bulk yield stress values at room temperature deduced from the estimated bulk CRSS values and the yield stresses obtained for polycrystals at high temperatures [20]. (b) Yield stresses normalized to shear modulus for various B2 single-phased compounds [60–63] plotted as a function of homologous temperature.

rate (1×10^{-4} s^{-1}) used in micropillar compression in the present study is an order of magnitude smaller than that (1×10^{-3} s^{-1}) used in compression for polycrystals in our previous study. The yield stress obtained at room temperature in micropillar compression (1792 MPa) could be much higher if micropillar compression was made at a strain rate of 1×10^{-3} s^{-1}. This indicates that the yield stress must be increased sharply with decreasing temperature below 673 K that corresponds to the lowest temperature for plastic flow. The room-temperature brittleness may stem from such a sharp increase in yield stress at room temperature. This is consistent with the interpretation based on the high BDTT, as discussed in the Section 4.1.

Yield stresses normalized to shear modulus for various B2 single-phased compounds [60–63] are plotted in Fig. 7(b) as a function of homologous temperature. The strain rate used for these measurements ranges from 1×10^{-4} to 2.1×10^{-4} s^{-1}. The 50Ti-35Mo-15Al high-entropy compound with the B2 structure is reported to exhibit <1 1 1> slip, although the slip plane was not unambiguously determined [63]. The normalized yield stresses for the two B2 high-entropy compounds, including TiCrMo-15Al are found to be much higher than those for the binary B2 compounds such as FeCo, FeAl and CuZn, all of which exhibit {1 1 0}<1 1 1> slip at room temperature. This must be due to significant solid-solution hardening in the B2 high-entropy compounds. These binary B2 compounds exhibit an anomalous increase in yield stress peaking at $0.45T/T_m$ (T_m is the melting temperature). However, this may not be the origin of the room temperature brittleness of the present case, as the yield stress is expected to rapidly increase with decreasing temperature at room temperature.

5. Conclusions

The plastic deformation behavior of a B2-ordered TiCrMo-15Al RHEA was investigated as a function of crystal orientation and specimen size by micropillar compression at room temperature. The results obtained are summarized as follows.

(1) Plastic flow is observed even at room temperature for all orientations investigated. The slip direction is always along <1 1 1>, while the slip plane is {1 1 0} in a wide orientation range, except for the large $|\chi|$ angles close to ± 30°, where the slip plane is {1 1 2}.

(2) The observed ψ-χ relationship indicates that {1 1 0} is the preferred slip plane. Twinning-anti-twinning asymmetry in yield stress is clearly observed; the CRSS for $(\bar{1}\ 0\ 1)[1\ 1\ 1]$ slip is higher for $\chi = -30°$ (the anti-twinning shear direction) than for $\chi = 30°$ (the twinning shear direction).

(3) The dislocation structure is characterized by the preference for <1 1 1> screw dislocations, strongly indicating that the deformation is controlled by the Peierls mechanism. The <1 1 1> dislocation is found to widely dissociate into two-coupled collinear 1/2<1 1 1> partial dislocations. From the dissociation width of the two-coupled super-partial dislocations, the APB energy is estimated to be 44 mJ/m^2, which is quite low and is considered to be the origin for the preference not only of the slip direction of <1 1 1> but also of the slip plane {1 1 0}.

(4) The room-temperature brittleness (limited ductility) of the present B2 intermetallic compound is considered not to be caused by the lack of the sufficient number of independent slip systems (von Mises criterion). We suspect that it is caused by the high brittle-ductile transition temperature (BDTT) in view of the preferential alignment of <1 1 1> dislocations along the Peierls valley parallel to their screw orientations, leading to the low dislocation mobility.

CRediT authorship contribution statement

Shu Han: Writing – review & editing, Writing – original draft, Visualization, Investigation, Funding acquisition, Validation. **Alexander Kauffmann:** Writing – review & editing, Funding acquisition. **Martin Heilmaier:** Writing – review & editing, Supervision, Funding acquisition, Conceptualization. **Haruyuki Inui:** Writing – review & editing, Supervision, Funding acquisition, Conceptualization. **Stephan Laube:** Writing – original draft, Visualization, Investigation. **Zhenghao Chen:** Writing – review & editing.

Declaration of Competing Interest

The authors declare that they have no known competing financial interests or personal relationships that could have appeared to influence the work reported in this paper

Acknowledgements

This work was supported by the Deutsche Forschungsgemeinschaft (DFG), grant no. HE 1872/34-2 and by the Japan Society for the Promotion of Science (JSPS) KAKENHI grant numbers JP22H00262, JP23K17338 and JP23KJ1302. SL specifically acknowledges the financial support for the research visit at Kyoto University by the DFG funded priority programme SPP 2006. The authors acknowledge the chemical analysis by ICP-OES at the Institute for Applied Materials (IAM-AWP), Karlsruhe Institute of Technology (KIT).

Data availability

No data was used for the research described in the article.

References

[1] O.N. Senkov, G.B. Wilks, J.M. Scott, D.B. Miracle, Mechanical properties of Nb25Mo25Ta25W25 and V20Nb20Mo20Ta20W20 refractory high entropy alloys, Intermetallics 19 (2011) 698–706, https://doi.org/10.1016/j.intermet.2011.01.004.

[2] D.B. Miracle, O.N. Senkov, A critical review of high entropy alloys and related concepts, Acta Mater. 122 (2017) 448–511, https://doi.org/10.1016/j.actamat.2016.08.081.

[3] O.N. Senkov, S. Gorsse, D.B. Miracle, High temperature strength of refractory complex concentrated alloys, Acta Mater. 175 (2019) 394–405, https://doi.org/10.1016/j.actamat.2019.06.032.

[4] T. Tsuru, S. Han, S. Matsuura, Z. Chen, K. Kishida, I. Iobzenko, S.I. Rao, C. Woodward, E.P. George, H. Inui, Intrinsic factors responsible for brittle versus ductile nature of refractory high-entropy alloys, Nat. Commun. 15 (2024) 1706, https://doi.org/10.1038/s41467-024-45639-8.

[5] O.N. Senkov, S.V. Senkova, C. Woodward, Effect of aluminum on the microstructure and properties of two refractory high-entropy alloys, Acta Mater. 68 (2014) 214–228, https://doi.org/10.1016/j.actamat.2014.01.029.

[6] O.N. Senkov, J.P. Couzinie, S.I. Rao, V. Soni, R. Banerjee, Temperature dependent deformation behavior and strengthening mechanisms in a low density refractory high entropy alloy Al10Nb15Ta5Ti30Zr40, Materialia 9 (2020) 100627, https://doi.org/10.1016/J.MTLA.2020.100627.

[7] V. Soni, B. Gwalani, T. Alam, S. Dasari, Y. Zheng, O.N. Senkov, D. Miracle, R. Banerjee, Phase inversion in a two-phase, BCC+B2, refractory high entropy alloy, Acta Mater. 185 (2020) 89–97, https://doi.org/10.1016/J.ACTAMAT.2019.12.004.

[8] Q. Wang, J. Han, Y. Liu, Z. Zhang, C. Dong, P.K. Liaw, Coherent precipitation and stability of cuboidal nanoparticles in body-centered-cubic Al0.4Nb0.5Ta0.5TiZr0.8 refractory high entropy alloy, Scr. Mater. 190 (2021) 40–45, https://doi.org/10.1016/J.SCRIPTAMAT.2020.08.029.

[9] J. Brodie, J. Wang, J.P. Couzinié, M. Heczko, V. Mazánová, M.J. Mills, M. Ghazisaeidi, Stability of the B2 phase in refractory high entropy alloys containing aluminum, Acta Mater. 268 (2024) 119745, https://doi.org/10.1016/J.ACTAMAT.2024.119745.

[10] S. Laube, S. Schellert, A. Srinivasan Tirunilai, D. Schliephake, B. Gorr, H.-J. Christ, A. Kauffmann, M. Heilmaier, Microstructure tailoring of Al-containing compositionally complex alloys by controlling the sequence of precipitation and ordering, Acta Mater. 218 (2021) 117217, https://doi.org/10.1016/j.actamat.2021.117217.

[11] Z.T. Kloenne, K. Kadirvel, J.-P. Couzinie, G.B. Viswanathan, Y. Wang, H.L. Fraser, High temperature phase stability of the compositionally complex alloy AlMo0.5NbTa0.5TiZr, Appl. Phys. Lett. 119 (2021), https://doi.org/10.1063/5.0069497.

[12] M.H. Yoo, T. Takasugi, S. Hanada, O. Izumi, Slip modes in B2-Type intermetallic alloys, Mater. Trans. JIM 31 (1990) 435–442, https://doi.org/10.2320/matertrans1989.31.435.

[13] M. Yamaguchi, Y. Umakoshi, The deformation behaviour of intermetallic superlattice compounds, Prog. Mater. Sci. 34 (1990) 1–148, https://doi.org/10.1016/0079-6425(90)90002-Q.

[14] M.J. Mills, D.B. Miracle, The structure of a⟨100⟩ and a⟨110⟩ dislocation cores in NiAl, Acta Metall. Mater. 41 (1993) 85–95, https://doi.org/10.1016/0956-7151(93)90341-O.

[15] A. Behgozin, T. Nakano, Y. Umakoshi, Fatigue, cyclic deformation and microstructure. Plastic deformation behaviour and substructure in CoTi single crystals fatigued at room temperature, ISIJ Int. 37 (1997) 1218–1223, https://doi.org/10.2355/isijinternational.37.1218.

[16] M. Yamaguchi, Y. Umakoshi, The operative slip systems and slip line morphology in βCuZn and β(CuNi)Zn alloys, Acta Met. 24 (1976) 1061–1067, https://doi.org/10.1016/0001-6160(76)90137-1.

[17] K. Yoshimi, S. Hanada, M.H. Yoo, On lattice defects and strength anomaly of B2-type FeAl, Intermetallics 4 (1996) S159–S169, https://doi.org/10.1016/0966-9795(96)80194-4.

[18] M. Yamaguchi, Y. Umakoshi, T. Yamane, Y. Minonishi, S. Morozumi, Slip systems in an Fe-54 at% Co alloy, Scr. Metall. 16 (1982) 607–609, https://doi.org/10.1016/0036-9748(82)90280-0.

[19] S. Laube, H. Chen, A. Kauffmann, S. Schellert, F. Müller, B. Gorr, J. Müller, B. Butz, H.J. Christ, M. Heilmaier, Controlling crystallographic ordering in Mo–Cr–Ti–Al high entropy alloys to enhance ductility, J. Alloy. Compd. 823 (2020) 153805, https://doi.org/10.1016/J.JALLCOM.2020.153805.

[20] S. Laube, G. Winkens, A. Kauffmann, J. Li, C. Kirchlechner, M. Heilmaier, Strength of disordered and ordered Al-containing refractory high-entropy alloys, Adv. Eng. Mater. (2024) 2301797, https://doi.org/10.1002/adem.202301797.

[21] S. Takeuchi, E. Furubayashi, T. Taoka, Orientation dependence of yield stress in 4.4% silicon iron single crystals, Acta Met. 15 (1967) 1179–1191, https://doi.org/10.1016/0001-6160(67)90392-6.

[22] S.S. Lau, J.E. Dorn, Asymmetric slip in Mo single crystals, Phys. Status Solidi A 2 (1970) 825–836, https://doi.org/10.1002/pssa.19700020420.

[23] C.R. Weinberger, B.L. Boyce, C.C. Battaile, Slip planes in bcc transition metals, Int. Mater. Rev. 58 (2013) 296–314, https://doi.org/10.1179/1743280412Y.0000000015.

[24] J. Mayer, L.A. Giannuzzi, T. Kamino, J. Michael, TEM sample preparation and FIB-induced damage, MRS Bull. 32 (2007) 400–407, https://doi.org/10.1557/MRS2007.63.

[25] D. Caillard, A TEM in situ study of alloying effects in iron. II—Solid solution hardening caused by high concentrations of Si and Cr, Acta Mater. 61 (2013) 2808–2827, https://doi.org/10.1016/j.actamat.2013.01.049.

[26] Dr.D. Caillard, A TEM in situ study of the softening of Tungsten by Rhenium, Acta Mater. 194 (2020) 249–256, https://doi.org/10.1016/j.actamat.2020.04.039.

[27] T. Yamagata, H. Yoshida, Y. Fukuzawa, Glide properties and dislocation structure of β-brass single crystals, Trans. JIM 17 (1976) 393–402, https://doi.org/10.2320/matertrans1960.17.393.

[28] H. Saka, M. Kawase, Dislocation structures of β-CuZn deformed in compression between 25 and 300°C, Philos. Mag. A 49 (1984) 525–533, https://doi.org/10.1080/01418618408236553.

[29] K. Yoshimi, S. Hanada, M.H. Yoo, On lattice defects and strength anomaly of B2-type FeAl, Intermetallics 4 (1996) S159–S169, https://doi.org/10.1016/0966-9795(96)80194-4.

[30] D.G. Morris, M.A. Morris, Dislocation processes leading to the stress anomaly in B2-type Fe-40%Al single crystals, Intermetallics 5 (1997) 245–263, https://doi.org/10.1016/S0966-9795(96)00095-7.

[31] G.B. Viswanathan, Z.T. Kloenne, J.-P. Couzinié, B.A. Welk, S.J. Kuhr, H.L. Fraser, Deformation mechanisms and their role in the lack of ductility in the refractory-based high entropy alloy AlMo0.5NbTa0.5TiZr, Acta Mater. 269 (2024) 119824, https://doi.org/10.1016/j.actamat.2024.119824.

[32] P.M. Anderson, J.P. Hirth, J. Lothe. Theory of Dislocations, 3rd ed., Cambrighe University Press, 2017.

[33] P.A. Flinn, Theory of deformation in superlattices, Trans. Met. Soc. AIME 218 (1960) 145–154.

[34] M.J. Marcinkowski, Electron Microscopy and Strength of Crystals, Interscience Publishers, 1963.

[35] D.I. Potter, Prediction of the operative slip system in CsCl type compounds using anisotropic elasticity theory, Mater. Sci. Eng. 5 (1970) 201–209, https://doi.org/10.1016/0025-5416(70)90082-0.

[36] H. Saka, M. Kawase, A. Nohara, T. Imura, Anti-phase boundary energy in β-CuZn, Philos. Mag. A 50 (1984) 65–70, https://doi.org/10.1080/01418618408244212.

[37] I.L.F. Ray, R.C. Crawford, D.J.H. Cockayne, The weak-beam technique applied to superlattice dislocations in an iron—aluminium alloy, Philos. Mag. 21 (1970) 1027–1032, https://doi.org/10.1080/14786437008238488.

[38] R.C. Crawford, I.L.F. Ray, Antiphase boundary energies in iron-aluminium alloys, Philos. Mag. 35 (1977) 549–565, https://doi.org/10.1080/14786437708235989.

[39] M. Rudy, G. Sauthoff, Dislocation creep in the ordered intermetallic (Fe, Ni)Al phase, Mater. Sci. Eng. 81 (1986) 525–530, https://doi.org/10.1016/0025-5416(86)90289-2.

[40] F. Popille, J. Douin, Comparison of the deformation microstructures at room temperature in O and B2 phases of a Ti2AlNb alloy, J. Phys. IV 06 (C2) (1996) 211–C2-216, https://doi.org/10.1051/jp4:1996229.

[41] O.N. Senkov, B. Crossman, S.I. Rao, J.P. Couzinie, D.B. Miracle, T.M. Butler, R. Banerjee, M. Mills, Mechanical properties of an Al10Nb20Ta15Ti30V5Zr20 A2/B2 refractory superalloy and its constituent phases, Acta Mater. 254 (2023) 119017, https://doi.org/10.1016/j.actamat.2023.119017.

[42] Y. Umakoshi, M. Yamaguchi, Y. Namba, K. Murakami, The effect of crystal orientation on the strength anomaly in β CuZn at around 200°C, Acta Met. 24 (1976) 89–93, https://doi.org/10.1016/0001-6160(76)90151-6.

[43] Y. Umakoshi, M. Yamaguchi, Deformation of FeAl single crystals at high temperatures, Philos. Mag. A 41 (1980) 573–588, https://doi.org/10.1080/01418618008239334.

[44] M. Yamaguchi, Y. Umakoshi, The Structure and Properties of Crystal Defects, Elsevier Science Pubilishers, 1984.

[45] M. Yamaguchi, Y. Umakoshi, The operative slip systems and slip line morphology in βCuZn and β(CuNi)Zn alloys, Acta Met. 24 (1976) 1061–1067, https://doi.org/10.1016/0001-6160(76)90137-1.

[46] Y. Umakoshi, M. Yamaguchi, Cross slip in βCuZn and β(CuNi)Zn alloys, Scr. Metall. 11 (1977) 909–913, https://doi.org/10.1016/0036-9748(77)90236-8.

[47] M. Yamaguchi, Y. Umakoshi, Slip geometry and anomalous strengthening in β-Cu(ZnMn) single crystals, Phys. Stat. Sol. A 43 (1977) 667–674, https://doi.org/10.1002/PSSA.2210430239.

[48] A.H. Cottrell, ed., Theoretical Structural Metallurgy, London, 1948.

[49] C. Sigli, J.M. Sanchez, Theoretical description of phase equilibrium in binary alloys, Acta Met. 33 (1985) 1097–1104, https://doi.org/10.1016/0001-6160(85)90203-2.

[50] M.O. Aboelfotoh, The operative slip systems and strain hardening behaviour of β′-AgMg single crystals, Phys. Stat. Sol. A 14 (1972) 545–559, https://doi.org/10.1002/pssa.2210140222.

[51] K. Kishida, H. Suzuki, M. Okutani, H. Inui, Room-temperature plastic deformation of single crystals of α-manganese - hard and brittle metallic element, Int. J. Plast. 160 (2023) 103510, https://doi.org/10.1016/J.IJPLAS.2022.103510.

[52] K. Kishida, Y. Shinkai, H. Inui, Room temperature deformation of 6H–SiC single crystals investigated by micropillar compression, Acta Mater. 187 (2020) 19–28, https://doi.org/10.1016/J.ACTAMAT.2020.01.027.

[53] K. Kishida, T. Maruyama, H. Matsunoshita, T. Fukuyama, H. Inui, Micropillar compression deformation of single crystals of Mo5SiB2 with the tetragonal D8l structure, Acta Mater. 159 (2018) 416–428, https://doi.org/10.1016/J.ACTAMAT.2018.08.048.

[54] S.-W. Lee, W.D. Nix, Size dependence of the yield strength of fcc and bcc metallic micropillars with diameters of a few micrometers, Philos. Mag. 92 (2012) 1238–1260, https://doi.org/10.1080/14786435.2011.643250.

[55] M.D. Uchic, D.M. Dimiduk, J.N. Florando, W.D. Nix, Sample dimensions influence strength and crystal plasticity, Science 305 (1979) (2004) 986–989, https://doi.org/10.1126/science.1098993.

[56] S. Korte, W.J. Clegg, Discussion of the dependence of the effect of size on the yield stress in hard materials studied by microcompression of MgO, Philos. Mag. 91 (2011) 1150–1162, https://doi.org/10.1080/14786435.2010.505179.

[57] H. Bei, S. Shim, G.M. Pharr, E.P. George, Effects of pre-strain on the compressive stress–strain response of Mo-alloy single-crystal micropillars, Acta Mater. 56 (2008) 4762–4770, https://doi.org/10.1016/J.ACTAMAT.2008.05.030.

[58] S.W. Lee, W.D. Nix, Size dependence of the yield strength of fcc and bcc metallic micropillars with diameters of a few micrometers, Philos. Mag. 92 (2012) 1238–1260, https://doi.org/10.1080/14786435.2011.643250.

[59] J.M. Rosenberg, H.R. Piehler, Calculation of the taylor factor and lattice rotations for bcc metals deforming by pencil glide, Metall. Trans. 2 (1971) 257–259, https://doi.org/10.1007/BF02662666.

[60] N.S. Stoloff, R.G. Davies, The plastic deformation of ordered FeCo and Fe3 Al alloys, Acta Met. 12 (1964) 473–485, https://doi.org/10.1016/0001-6160(64)90019-7.

[61] H. Xiao, I. Baker, The temperature dependence of the flow and fracture of Fe-40Al, Scr. Metall. Mater. 28 (1993) 1411–1416, https://doi.org/10.1016/0956-716X(93)90491-A.

[62] K.A. Lee, C.S. Lee, The effect of strain rate on the anomalous peak of yield stress in β-CuZn alloy, Scr. Mater. 39 (1998) 1289–1294, https://doi.org/10.1016/S1359-6462(98)00293-0.

[63] Y. Lu, J. Yamada, R. Miyata, H. Kato, K. Yoshimi, High-temperature mechanical behavior of B2-ordered Ti–Mo–Al alloys, Intermetallics 117 (2020) 106675, https://doi.org/10.1016/j.intermet.2019.106675.